WILEY | Hindawi

Research Article

Synthesis and Implementation of a Multiport Dual Input-Dual Output Converter for Electric Vehicle Applications

Reddi Khasim Shaik [ID] **and C. Dhanamjayulu** [ID]

School of Electrical Engineering, Vellore Institute of Technology, Vellore, Tamil Nadu, India

Correspondence should be addressed to C. Dhanamjayulu; dhanamjayulu.c@vit.ac.in

In recent years, multiport DC-DC converters are seen in a variety of power converter applications in electric vehicles. The design of multiport converter architectures plays a major role in DC microgrids and electric vehicle applications. This research examines a modified multiport converter structure interface with dual inputs and dual outputs used in electric vehicles. The versatility of accommodating energy sources with varying voltage and current nature characteristics is the most notable feature of this converter. During operation, the proposed architecture can offer a boost as well as buck operations at the same time. The suggested dual input-dual output (DIDO) converter is built with fewer components and a simpler control technique which makes it more dependable and the converter is cost-effective. Furthermore, this structure allows the power to flow in both directions making it to be utilized in electric vehicle battery charging during regenerative braking. The converter's steady-state and dynamic behavior are investigated, and a control strategy for regulating the power flow among the varied input energies is proposed. To develop the suggested converter, a small-signal model is modeled. MATLAB simulation and experimental findings are used for the verification of converter design and validated the performance behavior experimentally using a hardware setup.

1. Introduction

Electric vehicles (EVs) should be used instead of fossil-fuel cars because of the world's fast-expanding population and energy demand, raising the costs of gas and oil and the reduction of fossil fuels. As a result, enthusiasm for producing EVs powered by clean and renewable energy sources to replace fossil-fuel vehicles has constantly grown. Electric vehicles (EVs) are a promising alternative for transportation-related applications that may enable environmental operations by utilizing renewable energy sources [1, 2]. The solar PV system is utilized as a clean energy source in the case of electric vehicles. Solar PV energy sources produce electrical energy utilizing solar energy. The maximum power has been extracted from the solar panel by using the technique of maximum power point tracking (MPPT) [3]. At present, the adoption of solar PV energy systems meets the required demands in electric vehicle applications. These provide energy to the required load and charge the

battery as long as the energy is available. Hence, there exist many limitations of the solar PV system, such as the various irradiance levels causing the system less effective in power transfer to the load and the availability is not constant throughout the way. Hence, to overcome these limitations, the solar PV system along with a secondary source of battery is utilized to provide energy from source to load. The hybridized combination of energy storage systems provides a continuous power transfer to the load and meets the high-power requirements of the load during high speed and terrains [4–7]. The energy storage systems such as batteries and supercapacitors consist of different voltage ratings to interface them in the systems. Implementing the system with individual DC-DC converters for the respective source leads to the system being bulky and complex which makes the system costly. Hence, a converter along with various voltage-rated inputs is required to handle several energies and fed to the system. Hybrid energy storage systems are generally interfaced with a multi-input converter, which is of various

variants based on the isolation requirement concerning the nonisolation and isolation type DC-DC converters. The general layout representing the multi-input converter-fed electric motor is represented in Figure 1.

In an isolated multiport converter configuration, a transformer is employed with high frequency to produce isolation between the electric constraints. This provides efficient isolation and the matching of impedance among both sides of the converter. Leakage inductance is utilized as a storage device that stores energy in isolated converters to transmit the power among both sides of the converter. In addition to the high-frequency transformer, isolated dc-dc converters often comprise power converters. To maintain the efficient power transfer from both ports of the converter, the transformer phase shift among the primary and secondary voltage constraints has been changed [8–10]. These include various types of the converters such as half-bridge converters, full-bridge converters, and combinational multiport converters [11–13]. These are bulky because of the utilization of the transformer. The requirement of inverters in these converters is at the input port of the transformer with which the dc can be converted to ac supply and also the ac can be converter to dc by using the converters. Hence, there exist various switches utilized in all terminals of the converters increasing the losses with which the system losses get increased with the increase of transformer winding losses. These drawbacks are rectified in nonisolated multiport converters which are well-suited for electric vehicle applications.

A nonisolated multiport converter has been implemented concerning the H-bridge [14]. In practice, the various voltages can able to obtain by cascading H-bridge configurations by considering various dc-link voltage levels. The negative modes are not explored due to the coupling mechanism of the converter to the multiple ports [15]. The concept of a multiphase converter is first presented in [13, 16, 17]. The reduced order transfer function method is discussed in [18, 19] which is very advantageous with the higher order transfer function systems. By utilizing this method, the design of the controller becomes simple and the analysis gets simplified. The energy can be absorbed as well as delivered among the load from the energy storage sources of the converter. There exists an individual inductor for each source, and hence, this is considered a drawback of the converter. The author offers a three-input converter for the connection of batteries, solar cells, and fuel cells. With correct converter switching, you may charge and discharge the battery from various sources and loads. A systematic technique for designing nonisolated topologies is presented in [20] using a mix of buck type, boost type, sepic, and cuk type converters. Two types of converters are described such as PVSC and PCSC which are pulsing voltage and current sources, respectively. PVSC can be linked with the inductor in series to form a double-input converter as it represents a voltage source. Because the PCSC is a current source, it may be used to build a double-input converter by connecting it in series with a capacitor. In [21, 22], various heuristic dynamic programming techniques are proposed, and with the increase of the number of outputs to the load, the complexity

of the system gets implemented. In this case, the adaptive dynamic programming approach is essential to simplify the analysis and to design an efficient control technique. The energy management strategy, among the various inputs such as battery, SC, and the electric motor, is suggested for use in an electric automobile. Here, instead of employing two separate inductors as energy, storage components are used. When compared to two independent inductors, it is claimed that employing the inductors with coupling can save 22–26% in volume. Connected inductors, on the contrary, have a larger volume than a single inductor. This converter also enables braking energy regeneration to the battery and SC [23] and proposes that load power be transferred across input sources using a multiport converter with a single inductor. This converter can also be used to transport power between sources. In [24], the author introduced a revolutionary single-stage multiport converter that is expandable. The layout of conventional converters utilized in electric vehicles is represented in Figure 1(a) whereas the proposed converter configuration is represented in Figure 1(b).

Handling the low torque ripple plays a vital role in electric cars. Torque ripple in ac motors is related to voltage harmonics, and these can be minimized with the utilization of multilevel inverters. To create multilayer voltage, multilevel inverters require dc excitations with equal or different values of voltages. Multiple dc-links can be generated using multiport converters. Naik et al. and Rekik et al. [24, 25] offer a multiport converter that may create numerous voltages at its output sections, and these are the preset values regardless of the variation of the load power and input voltage. Podder et al. [26] present a novel multi-output buck converter control technique that delivers suitable dynamic performance. However, this converter is worthless in applications such as electric cars, where various input energy excitations, such as solar and a battery, are utilized. This can be solved by incorporating multi-port converters. Babaei et al. and Chittathuru et al. [27, 28] present a nonisolated single inductor multi-port converter. This converter's downside is that it employs a high switch count with low efficiency. The suggested converter's inability to transmit energy across input sources is another flaw.

A novel multi-port nonisolated DIDO or D^2-M^2 converter is suggested in this work, which is based on the mixture design of multiple inputs and outputs of the converter. In comparison to previous scenarios, the suggested converter contains fewer components. This converter can regulate the flow of electricity between sources and loads. Furthermore, the suggested converter includes many outputs, each of which can have a different voltage level. The suggested converter has benefits like a modular structure with fewer components and integration of several sources with various voltage-current characteristics in the input. In addition to the capabilities mentioned above, the proposed converter can produce output that is either more than the maximum input voltage or lower than the minimum input voltage (buck) (boost). The efficiency of the suggested converter is increased by lowering switching losses.

The following is a breakdown of the paper's structure. The main idea for designing DIDO and its operation modes
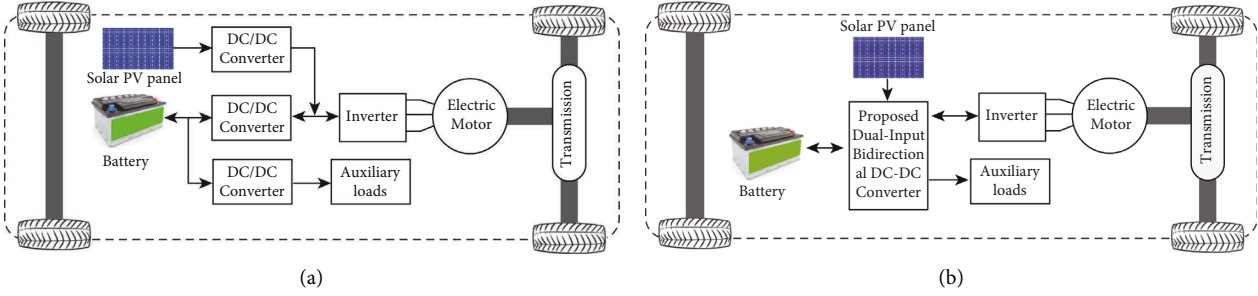
FIGURE 1: Block diagram representing conventional and proposed converter.

is described in Section 2. Section 3 presents the converter's dynamic model utilizing small-signal analysis. In Sections 4 and 5, the suggested converter's functions are validated using experimental data and a power budgeting control technique. Finally, Section 6 has the conclusion.

2. Performance Analysis of DIDO Converter

2.1. DIDO Converter Configuration. As the power requirement in the electric vehicle is varying concerning time, a single energy input cannot meet the requirement of the load. As a result, the combination of various energy sources is necessary. The goal of this study is to create a converter architecture that can connect diverse energy sources to a vehicle's motor train. Figures 1(a) and 1(b) show the layout of power converter components interfaced in an electric vehicle. The following are some of the most notable characteristics of the suggested converter:

Bidirectional power flow capabilities

Power flow control among the sources to load

Design and control should be simple

The adjustable switches S_1, S_2, and S_3 govern the power flow between the load and the input sources, as represented in Figure 2. The suggested structure can be examined in five operating states represented in Figures 3(a)–3(e). In the first state of operation, single input is provided to the circuit and dual outputs are at the load. The drive train of an electric vehicle (load) is powered by PV power shown in Figure 3(a). In the suggested topology, the battery can be charged either from PV power or from the load represented in Figures 3(b)–3(e).

The energy from the load can be stored in the battery due to regenerative braking in condition 5. If solar PV cannot generate enough electricity due to low irradiation, the battery discharges to meet the total desired load shown in Figure 3(c). Both battery and PV give the required electricity for the drive train at peak power demand. The converter subsequently enters the DIDO mode of operation (see Figure 3(d)). Figures 4 and 5 show the proposed converter's switching schemes as well as similar circuits in various operational states.

2.2. Modes of Operation of the Proposed DIDO Converter

2.2.1. Mode 1: PV to Load. In this stage, the power from the solar PV energy source transfers to the load independently. The switching strategies of the controlled switches are
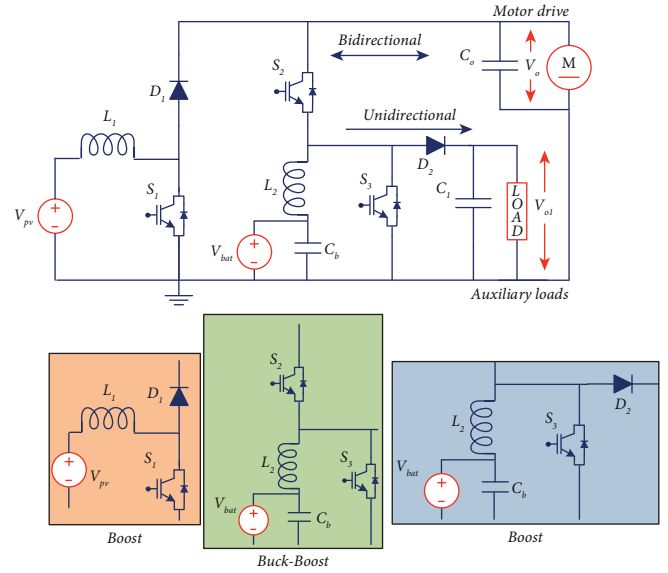

FIGURE 2: Proposed dual-input dual-output (DIDO) converter.

represented in Table 1. Switches S_1 and S_3 are turned on and S_2 is switched off for 0 to $d_1 T_s$ time interval. When $V_{pv} > V_{bat}$, the voltage V_{pv} occurs across the inductor L_1, resulting in a positive slope rise in the inductor current. During the time interval $d_1 T_s$ to T_s, switches S_1, S_3, and S_2 are turned on and off represented in Figure 3(a) and 3(b). Energy stored in inductor L_1 during the previous period $d_1 T_s$ is discharged to the output capacitor through the diode D_1. T_s stands for the transition period. In steady-state operation, the output voltage is given by

$$V_0 = \frac{1}{1 - d_1} V_{pv},$$

$$V_{01} = \frac{1}{1 - d_1} V_{pv}. \tag{1}$$

2.2.2. Mode 2: PV to Battery and Load. This mode of operation is similar to state 1. S_2 operates with d_2 0 : 5 to charge the battery when it is charged from solar PV represented in Figures 3(c) and 3(d). S_3 produces boosted output across the load in the same way as S_1 does, with $d_1 > 0.5$. The equations for the respective input and output port parameters are represented below:
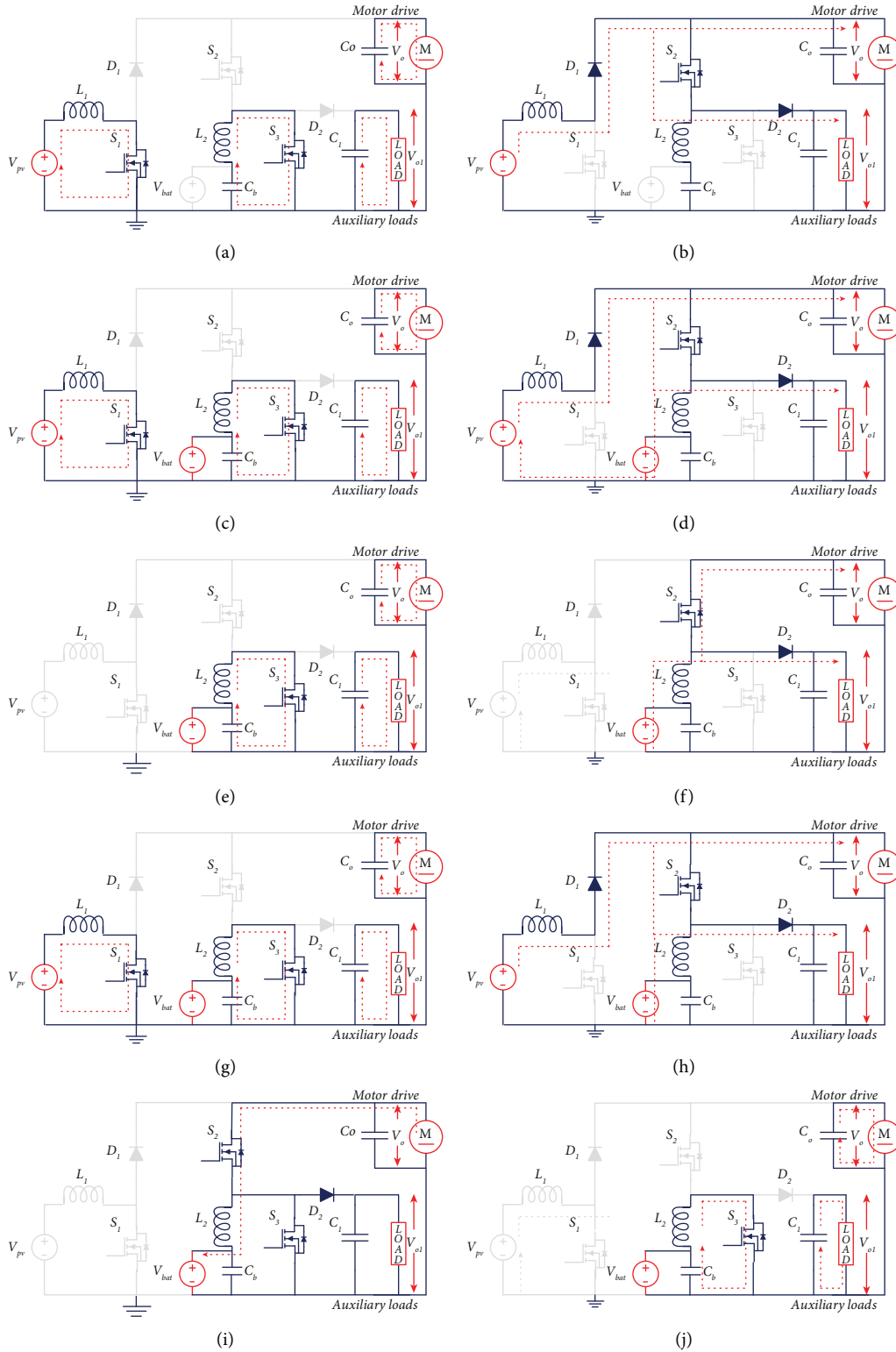
FIGURE 3: Modes of operation for all states.

$$V_0 = \frac{1}{1 - d_1} V_{pv},$$

$$V_{01} = d_2 V_{pv}, \tag{2}$$

$$V_{bat} = d_2 V_{pv}.$$

2.2.3. Mode 3: Battery to Load. During this mode of operation, the battery discharges the stored energy and is fed to the load. The energy discharge and the variation of the inductor current are at 0 to $d_3 T_s$ time intervals. The negative slope arises between the intervals $d_3 T_s$ and T_s where the current I_{L2} gets decreased. The switch S_3 provides a boosted
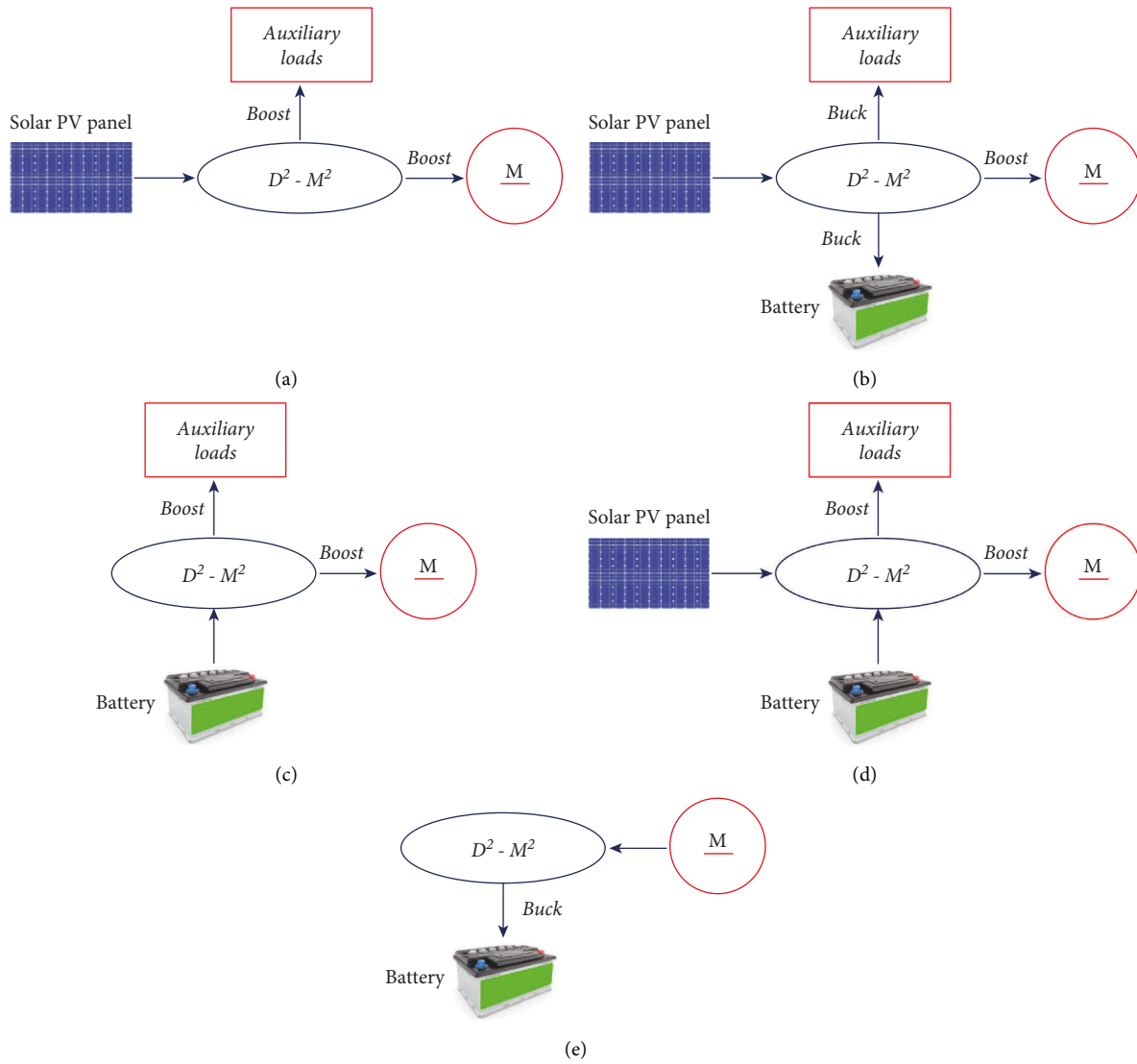
FIGURE 4: Typical representation of all states of operations. (a) State-1, (b) State-2, (c) State-3, (d) State-4 and (e) State-5.
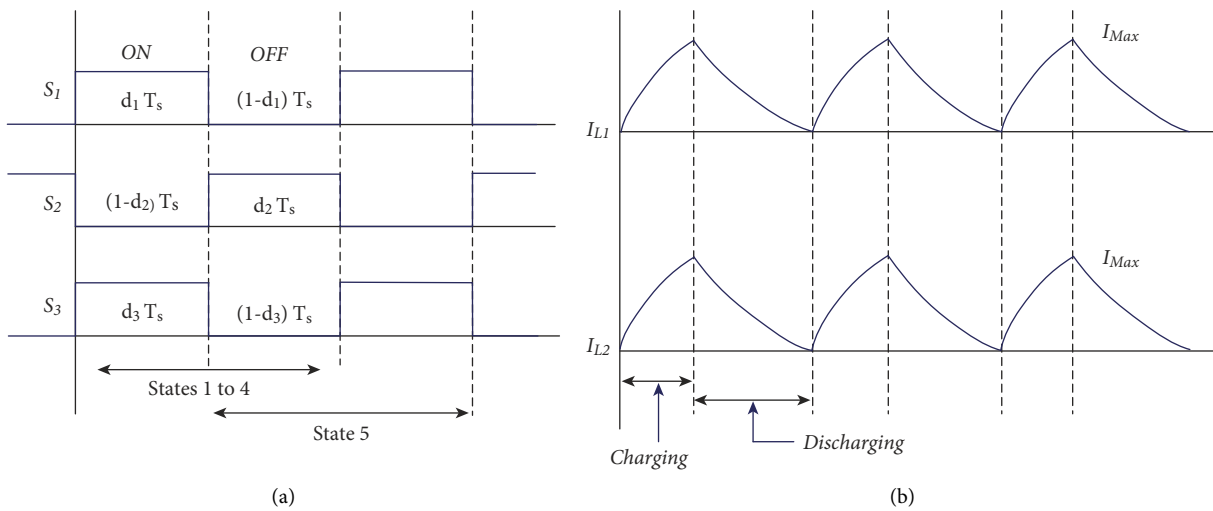

FIGURE 5: Typical waveforms of PWM signal and inductor current.

TABLE 1: Modes of operation of the proposed DIDO converter.

No. of states	Input sources	Switches			Inductors		Diodes		Battery	Capacitors		Outputs	
		S_1	S_2	S_3	$L1$	$L2$	D_1	D_2	V_{bat} or C_b	C_0	C_1	V0	V_{01}
Mode 1	V_{pv} or V_{dc}	✓	—	✓	C	C	—	—	—	D	D	Boost	Boost
		—	✓	—	D	D	✓	✓	—	C	C		
Mode 2	V_{pv} or V_{dc}	✓	—	✓	C	D	—	—	C	D	D	Boost	Boost
		—	✓	—	D	C	✓	✓	C	C	C		
Mode 3	V_{bat}	—	—	✓	—	C	—	—	D	D	D	Boost	Boost
		—	✓	—	—	D	—	✓	D	C	C		
Mode 4	V_{pv} and V_{bat}	✓	—	✓	C	C	—	—	D	D	D	Boost	Boost
		—	✓	—	D	D	✓	✓	D	C	C		
Mode 5	During regeneration	—	✓	—	—	C	—	✓	C	D	D	Buck	Buck
		—	—	✓	—	D	—	—	C	C	C		

output to the drive train during its ON-OFF state process. Because S_1 does not participate in the energy transfer from battery to load and remains to be turned off during the operation represented in Figures 3(e) and 3(f), the load voltage discharging from the battery is given by

$$V_0 = \frac{1}{1 - d_3} V_{bat},$$

$$V_{01} = \frac{1}{1 - d_3} V_{bat}. \tag{3}$$

2.2.4. Mode 4: PV and Battery to Load. Whenever the requirement of energy is high to meet the desired load, the battery and PV systems provide enough energy to satisfy the demand represented in Figures 3(g) and 3(h). S_1 and S_3 switches can charge the inductor, and the inductor currents i_{L1} and i_{L2} get increased during 0 to $d_1 T_s$ time interval. S_2 is given with the complementing gate signal at this period. During the off period of switches S_1 and S_3, on the contrary, the currents i_{L1} and i_{L2} fall with a negative slope. Diodes D_1 and D_2 deliver power from both input sources to the load. The net output voltage is given by

$$V_0 = \frac{1}{1 - d_3} V_{pv},$$

$$(\text{or})V_0 = \frac{1}{1 - d_3} V_{bat}, \tag{4}$$

$$V_{01} = \frac{1}{1 - d_1} V_{pv},$$

$$(\text{or})V_0 = \frac{1}{1 - d_3} V_{bat}. \tag{5}$$

2.2.5. Mode 5: Load to Battery. The battery gets charged from the energy from the power train during regenerative braking represented in Figures 3(i) and 3(j). The following is the switching for this state: S_1 is always turned off, S_3 and S_2 are turned on and off, respectively, and Q_2 is ON state, as well as S_3 charges the battery:

$$V_{bat} = d_2 V_0. \tag{6}$$

The battery is supplied via regenerative braking power in the same state. The control relationship is deduced as follows:

$$V_{01} = d_3 V_0. \tag{7}$$

3. Dynamic Modelling

To manage the output voltages and the charging and discharging activities of the battery, a proper control system is necessary for each switch in the converter. Because of this, a small-signal model of the converter is needed to develop such controllers. The four-port converter's state-space average model is constructed from the state-space description of the converter in each state of switching. Determining an average model is done as follows. The state-space equations are derived for each switching state of the switches. The steps involved in deducing the state-space model are using perturbation and matrix creation methods.

To create the small-signal model, the current flowing through the inductors and the voltage across the capacitors are treated as state variables. Many distinct models can be created because of the given converter's operating states that use different combinations of the input sources to create either buck, boost, or buck-boost outputs at the same time. Element components (I, d, V) and perturbations are used to construct the state variables in equation (8) Perturbations are thought to fluctuate modestly during a single switching phase. Replace the state parameters with the sum of steady-state and perturbation values to create the following restrictions:

$$
\begin{aligned}
i_{L_1} &= I_{L_1} + \overline{I_{L_1}}, \\
i_{L_2} &= I_{L_2} + \overline{I_{L_2}}, \\
V_0 &= V_0 + \overline{V_0}, \\
V_{01} &= V_{01} + \overline{V_{01}}, \\
V_{bat} &= V_{bat} + \overline{V_{bat}}, \\
d_1 &= d_1 + \overline{d_1}, \\
d_2 &= d_2 + \overline{d_2}, \\
d_3 &= d_3 + \overline{d_3}.
\end{aligned}
\tag{8}
$$

3.1. Mode 1: PV to Load. The switches in Figures 3(a) and 3(b) are used to indicate that the converter is in CCM mode. For a time of $d_1 T_s$, S_1 is ON, S_2 is OFF, and S_1 is OFF, and S_2 is ON $(1 - d_1 T_s)$. It is feasible to obtain by substituting the perturbations:

$$\frac{d\overline{V_0}}{dt} = \left(\frac{1 - d_1}{C_0}\right)\overline{I_{L_1}} - \left(\frac{d_1}{C_0}\right)I_{L_1} - \left(\frac{1}{C_0 r_0}\right)\overline{V_0},$$

$$\frac{d\overline{V_{01}}}{dt} = \left(\frac{1 - d_1}{C_1}\right)\left(\overline{I_{L_1}} + \overline{I_{L_2}}\right) - \left(\frac{d_1}{C_1}\right)\left(\overline{I_{L_1}} + \overline{I_{L_2}}\right) - \left(\frac{1}{C_1 r_1}\right)\overline{V_{01}},$$

$$\overline{d_1} I_{L_1} = (1 - d_1)\overline{I_{L_1}} - \left(C_0 + \frac{1}{r_0}\right)\overline{V_0},$$

$$\overline{d_1} I_{L_1} = (1 - d_1)\left(\overline{I_{L_1}} + \overline{I_{L_2}}\right) - \left(C_1 + \frac{1}{r_1}\right)\overline{V_{01}},$$

(9)

$$\frac{1}{\overline{d_1}} = \begin{bmatrix} \overline{I_{L_1}} \\ \overline{V_0} \\ \left(\overline{I_{L_1}} + \overline{I_{L_2}}\right) \\ \overline{V_{01}} \end{bmatrix} = \begin{bmatrix} L_1 & (1 - d_1) & 0 & 0 \\ (1 - d_1) & \left(C_0 + \frac{1}{r_0}\right) & 0 & 0 \\ 0 & 0 & (L_1 + L_2) & (1 - d_1) \\ 0 & 0 & (1 - d_3) & \left(C_1 + \frac{1}{r_1}\right) \end{bmatrix}^{-1} \times \begin{bmatrix} I_{L_1} \\ V_0 \\ \left(I_{L_1} + I_{L_2}\right) \\ V_{01} \end{bmatrix}.$$

(10)

3.2. Mode 2: PV to Battery and Load. S_1 and S_3 remain ON in this state, while S_2 remains OFF, as shown in Figure 3(c) and 3(d). The perturbations are incorporated as follows:

$$\frac{d_1 (V_0 + \overline{V_0})}{dt} = \left(\frac{1 - d_1 - \overline{d_1}}{C_0}\right)\left(I_{L_1} + \overline{I_{L_1}}\right) - \left(\frac{1}{C_0 r_0}\right)(V_0 + \overline{V_0}),$$

$$\frac{d_2 (V_{01} + \overline{V_{01}})}{dt} = \left(\frac{1}{C_0}\right)\left(I_{L_2} + \overline{I_{L_2}}\right) - \left(\frac{1}{C_1 r_1}\right)(V_{01} + \overline{V_{01}}),$$

(11)

$$\frac{d_2 (V_{bat} + \overline{V_{bat}})}{dt} = \left(\frac{1}{C_b}\right)\left(I_{L_2} + \overline{I_{L_2}}\right) - \left(\frac{1}{C_b}\right)(V_{bat} + \overline{V_{bat}}),$$

$$\frac{1}{\overline{d_1} \& \overline{d_2} \& \overline{d_3}} \begin{bmatrix} \overline{I_{L_1}} \\ \overline{I_{L_2}} \\ \overline{V_0} \\ \overline{V_{bat}} \\ \overline{V_{01}} \end{bmatrix} = \begin{bmatrix} L_1 & 0 & (1 - d_1) & 0 \\ 0 & 0 & 0 & -d_2 \\ (1 - d_1) & 0 & -\left(C_0 + \frac{1}{r_0}\right) & 0 \\ 0 & -1 & 0 & -1 \\ (1 - d_3) & 0 & -\left(C_1 + \frac{1}{r_1}\right) & 0 \end{bmatrix}^{-1} \times \begin{bmatrix} V_0 \\ V_{bat} \\ V_{01} \\ I_{L_1} \\ I_{L_2} \end{bmatrix}.$$

(12)

3.3. Mode 3: Battery to Load. The switch S_3 is on and S_2 is off in this state, and the inductor L_2 is charged. Figures 3(e) and 3(f) show that switch S_3 is turned off and switch S_2 is turned on, and inductor L_2 is drained. The following are examples of small-signal equations that are inferred:

$$\frac{1}{\overline{d_1}} \begin{bmatrix} \overline{I_{L_2}} \\ \overline{V_{01}} \\ \overline{V_0} \end{bmatrix} = \begin{bmatrix} L_2 & (1-d_3) & 0 \\ (1-d_3) & \left(C_1 + \dfrac{1}{r_1}\right) & 0 \\ 0 & (1-d_3) & \left(C_0 + \dfrac{1}{r_0}\right) \end{bmatrix}^{-1} \times \begin{bmatrix} I_{L_2} \\ V_{01} \\ V_0 \end{bmatrix}. \quad (13)$$

3.4. Mode 4: PV and Battery to Load. State 4 combines the operations of states 1 and 3 represented in Figures 3(g) and 3(h), and the average converter model with the switching sequence shown in Table 1 can be obtained as

$$\frac{1}{\overline{d_1} \& \overline{d_3}} \begin{bmatrix} \overline{I_{L_1}} \\ \overline{V_0} \\ \overline{I_{L_2}} \\ \overline{V_{01}} \end{bmatrix} = \begin{bmatrix} L_1 & (1-d_1) & 0 & 0 \\ (1-d_1) & \left(C_0 + \dfrac{1}{r_0}\right) & 0 & 0 \\ 0 & 0 & L_2 & (1-d_3) \\ 0 & 0 & (1-d_3) & \left(C_0 + \dfrac{1}{r_1}\right) \end{bmatrix}^{-1}$$
$$\times \begin{bmatrix} I_{L_1} \\ V_0 \\ I_{L_2} \\ V_{01} \end{bmatrix}. $$
$$(14)$$

3.5. Mode 5: Load to Battery. Because the load power is negative, this state is referred to as regenerative. S_1 is turned off, and S_2 and S_3 are adjusted as illustrated in Figures 3(i) and 3(j) to store the regenerative braking energy in the battery. Because the output voltage is greater than V_{pv} during regenerative operation, the converter functions in buck mode and charges the battery. The small-signal model can be deduced by averaging the state equations over one period, as shown in the equation below:

$$\frac{d\left(I_{L_2} + \overline{I_{L_2}}\right)}{dt} = \left(\frac{d_2 - \overline{d_2}}{L_2}\right) V_{\text{brake}} - \left(\frac{1}{L_2}\right)(V_{\text{bat}} + \overline{V_{\text{bat}}}),$$

$$\frac{d\left(V_0 + \overline{V_0}\right)}{dt} = \left(\frac{I_{L_2} + \overline{I_{L_2}}}{C_b}\right) - \left(\frac{V_{\text{bat}} + \overline{V_{\text{bat}}}}{C_b}\right),$$

$$\frac{d\left(\overline{I_{L_2}}\right)}{dt} = -\frac{V_{\text{bat}}}{L_2} - \frac{\overline{V_{\text{bat}}}}{L_2},$$

$$\frac{d\left(\overline{V_{\text{bat}}}\right)}{dt} = \left(\frac{I_{L_2} + \overline{I_{L_2}}}{C_b}\right) - \left(\frac{\overline{V_{\text{bat}}}}{C_b}\right),$$

$$(15)$$

$$\frac{1}{\overline{d_2}} \begin{bmatrix} \overline{I_{L_2}} \\ \overline{V_{\text{bat}}} \end{bmatrix} = \begin{bmatrix} -L_2 & -1 \\ -1 & (1+C_b) \end{bmatrix}^{-1} \times \begin{bmatrix} I_{L_2} \\ V_{\text{bat}} \end{bmatrix}. \quad (16)$$

In summary, the five operational states are explained, and the closed-loop analysis of the proposed DIDO converter is performed using the small-signal model of the transfer function (output voltage/duty cycle).

4. Control Strategy and Hardware Results

A solar panel of 100 W consisting of two monocrystalline 50 W PV panels is considered the primary source, and a 12 V, 7 Ah battery is considered the storage element. To determine the maximum power point, the solar panel is equipped with a traditional P&O MMPT controller. The developed converter is designed and implemented in hardware represented in Figure 11(e), and Figure 9 represents the various modes of operation for various states. Table 2 shows the experimental specifications. MOSFETs (IRFP250 N) switches are utilized in the developed topology. The switch and state selection control algorithms are shown in Figures 5(a) and 5(b). The flowchart of energy management is represented in Figure 6. The duty cycles of the MOSFETs S_1, S_2, and S_3 are generated using a basic PI controller; Figure 7 represents the duty cycles of S_1, S_2, and S_3. To determine the current references, the reference output voltages (V_{o_ref} and V_{01_ref}) are compared to the real load output voltages (V_0 and V_{01}) and an error is generated (I_{L1ref} and I_{L2ref}). The PI controller's k_p and k_i parameters were discovered using MATLAB. The reference signals of the S_1 and S_2 duty cycles are determined by the current error. The duty cycles of S_1 and S_2 are calculated by comparing the 10 kHz carrier signal with the reference signal. S_1 and S_3 are operated at the same time with the same duty cycle, whereas S_2 is operated in a complementary manner.

4.1. Mode 1 and 2. The controller processes the feedback states and then delivers the duty cycles to operate the converter under a certain condition shown in Figure 10. If $V_{pv} > V_{bat}$, the controller evaluates V_{pv} and V_{bat} and selects states 1 and 2. Switch S_1 is triggered based on the PWM technique after state selection and the converter runs in SIDO mode. The output voltage V_0 and V_{01} is 67 V.

4.2. Mode 3. If V_{pv} and V_{bat} are set, mode 3 has opted and operates in the same way as state 1 with the battery as the primary power source. As indicated in Figure 11, the battery (where V_{bat} is 12 V and I_{bat} is 8 A) that was charged in the past cycle now drains to generate an increased output: V0 and V_{01} are 56 V and, I_{out} is 1 A.

4.3. Mode 4. When V_{pv} and V_{bat} occur, the converter is in mode 4. The load is powered by the primary source (V_{pv}) and the battery to satisfy the predicted demand. Figure 11 shows the experimental results for this stage of operation. When V_{pv} is 20 V, I_{pv} is 4.8 A, V_{bat} is 20 V, I_{bat} is 4.8 A, and V_0 and V_{01} are 36 V.

4.4. Mode 5. When the power exceeds the input power, the state changes in the process of regenerative braking. The motor drive oppositely provides energy. Due to the
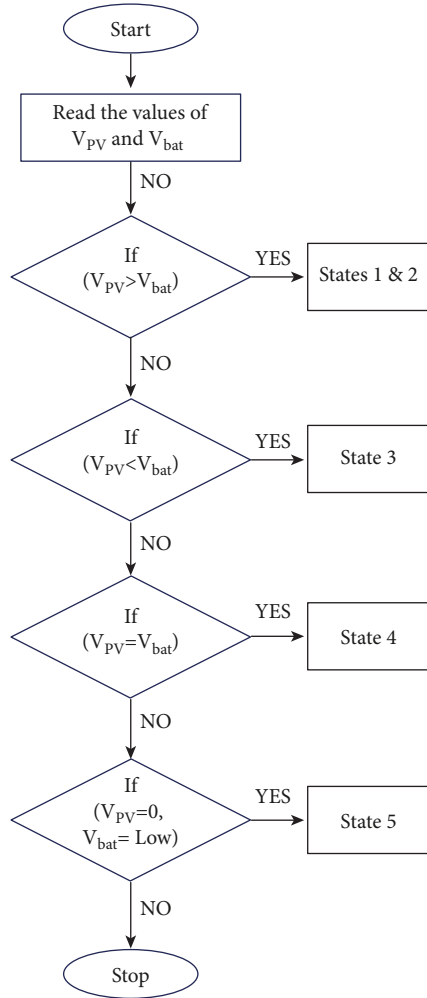
FIGURE 6: Flowchart for the proposed converter control strategy.

TABLE 2: Setup configuration.

Components	Ratings
Capacitor (C_1 and C_0)	63 V, 100 uF
Diode (D_1 and D_2)	UF5408
MOSFET	IRFP250 N
Battery	12 V, 7 Ah
Inductor (L_1)	1 mH
Inductor (L_2)	120 uH
dSPACE	RTI1104
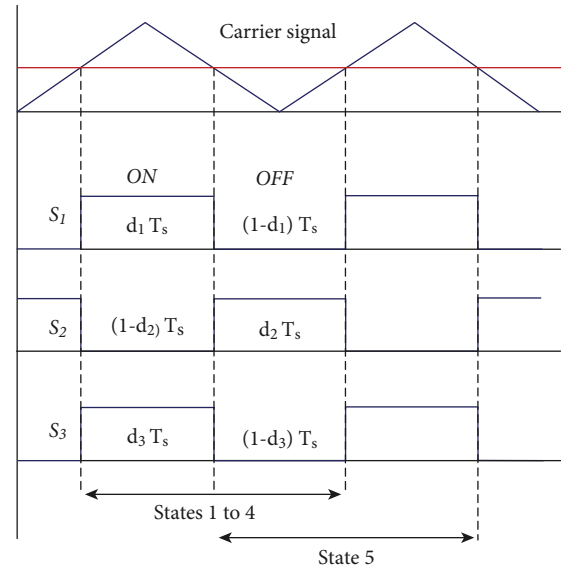
FIGURE 7: Duty cycle of the proposed converter with its carrier frequency.

converter's bucking activity, the energy from the brake is drawn and the battery gets charged. Figure 11 shows the charging parameters such as voltage and current: V_{bat} are 10.2 V and I_{bat} is 9.3 A when V_0 (brake) is 34 V and I_0 (brake) is 2.8 A.

The converter should have a higher degree of control freedom when used in an electric car. With this goal in mind, the converter is put through its paces with various duty cycles. Based on the results, it is clear that the suggested converter has a greater degree of control freedom and can give a higher output voltage.

For instance, in mode 1 represented in Figure 10, the input voltage is reduced from 22 to 20 V and then abruptly boosted to a value of 25 V greater than the supplied input voltage. The duty ratios d_1 and d_2 control buck and boosted voltages. Figure 11 illustrates the controller's capacity to correct for a 9% fall in input voltage and a 14% rise in input voltage using the idea of line regulation. Figure 11 shows the controller's load regulation performance against a 20% rise in the step-and-step drop-in R_{01}. This demonstrates that the planned controller can maintain outputs of 42.81 V and 42.67 V across both loads regardless of load or input variations.

4.4.1. Battery SoC and SoH Measurement. The battery gets discharged to the load in modes 3 and 4 and the load supplies power to the battery in mode 5. The developed configuration is carried out experimentally along with a battery SOC of 45.1256% at the start. The SOC of the battery gradually decreases during state 3 and state 4 (battery discharges). At the end of stage four, the measured SOC is 45.0345%. Because the states operate for such a short time and are exercised at such a high-switching frequency interval, the change in SOC is quite modest. Similarly, the battery SOC has been raised from 45.0345 to 45.0526% during mode 5. The SOH values are also calculated as 80.001 to 8.002 from mode 1 to the conclusion of mode 5. The proposed DIDO converter is compared with the various existing topologies and presented in Table 3 whereas the graphical representation is presented in Figure 12. The simulation and experimental results for various irradiances are represented in Figures 8 and 9, respectively.

5. Efficiency-Loss Analysis

Switching losses can be evaluated under various modes of operations using a standard buck, boost, or buck-boost converter considered as a reference. There are no additional losses because the developed converter acts as a standard
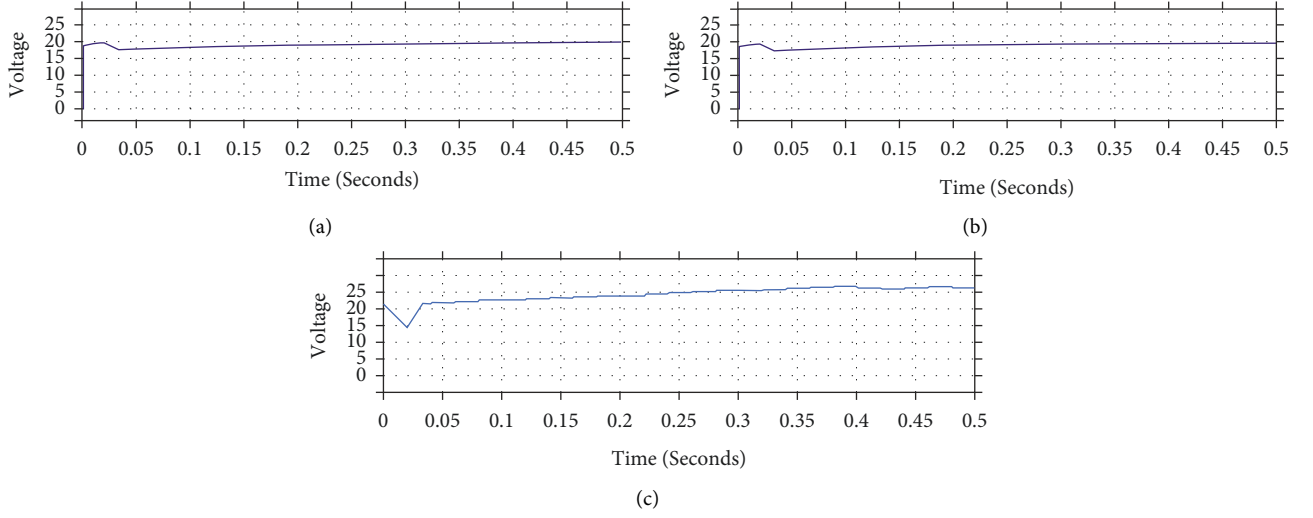
(a)

(b)

(c)

FIGURE 8: Simulation results of PV irradiance variation. (a) 490 W/m2, (b) 660 W/m2, (c) 1000 W/m2
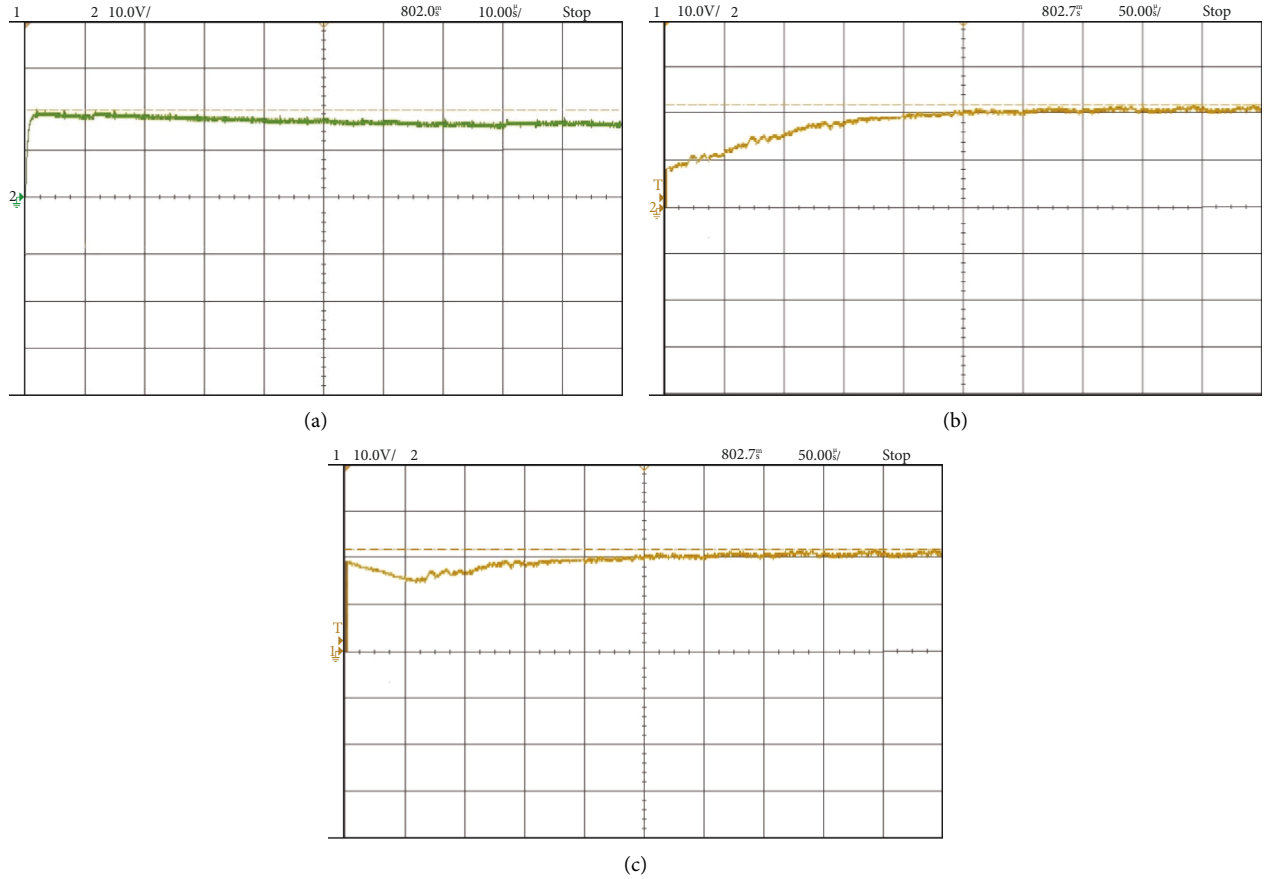

(a)

(b)

(c)

FIGURE 9: Experimental results of PV irradiance variation. (a) 490 W/m^2. (b) 660 W/m^2. (c) 1000 W/m^2.

boost converter in modes 3 and 4, and a buck converter in mode 5. As a result, the comparative change in efficiency for states 1 and 2 must be determined separately. The increased conduction loss owing to S_2 can be represented as in mode 1, whenever the converter acts as a general boost converter:

$$\Delta_{P_{\text{LOSS1}}} = \Delta_{P_{Q_2}} \text{ (boost)}. \tag{17}$$

Similarly, in mode 2, the developed converter functions in buck mode, charging the battery from the solar PV energy source and interconnecting the load and PV in boost mode. As a result, a loss change may be calculated as

$$\Delta_{P_{\text{LOSS2}}} = \Delta_{P_{Q_2}} \text{ (boost)},$$
$$\Delta_{P_{\text{LOSS2}}} = \Delta_{P_{D_1}} + \Delta_{P_{Q_1}} \text{ (buck)}. \tag{18}$$

X-axis: Time (sec)
Y-axis: Solar PV &
Battery Voltage (V)

(a)

X-axis: Time (sec)
Y-axis: Inductor
current & Duty cycle

(b)

X-axis: Time (sec)
Y-axis: Output Voltage (V)

(c)
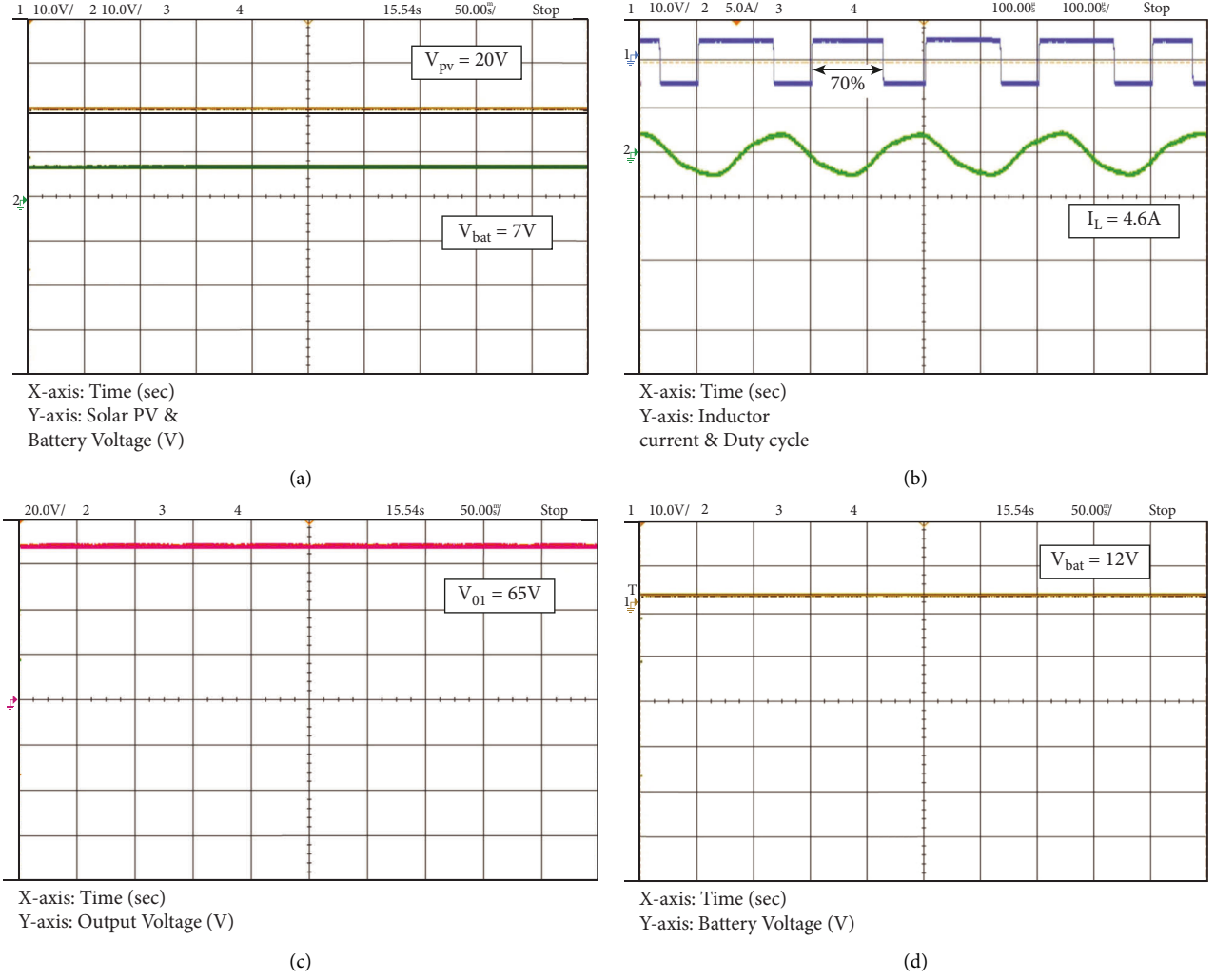
X-axis: Time (sec)
Y-axis: Battery Voltage (V)

(d)

FIGURE 10: Experimental results of the proposed DIDO converter for state-1 and state-2 operation. (a) Solar PV and battery input voltage. (b) Duty cycle and inductor current. (c) Output voltage. (d) Battery voltage.

Hence, efficiency is calculated with the following equation:

$$\Delta\eta = \eta - \eta' = \frac{P_O}{P_{IN}} - \frac{P_O}{P_{IN} + \Delta P_{LOSS}}. \quad (19)$$

Here, the above equation represents the efficiency of a traditional buck-boost type converter and 0 represents the efficiency of a developed buck-boost converter. The input and output power are denoted by the letters P_{IN} and P_O, respectively.

State 1: during boost mode,

$$\Delta\eta_1 = \eta_1 - \eta'_1,$$
$$\Delta\eta_1 = 0.9785 - 0.9748 = 0.37\%. \quad (20)$$
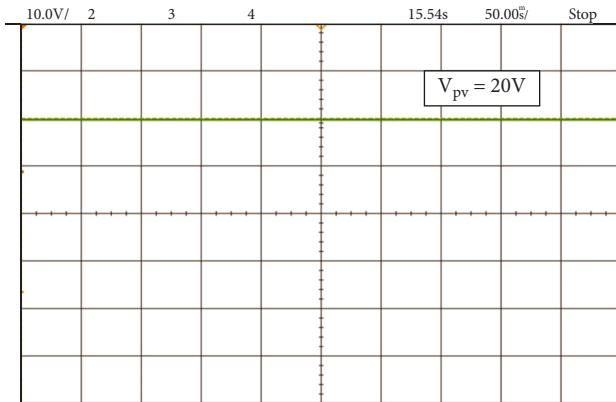
State 2: during boost mode,

$$\Delta\eta_1 = \eta_1 - \eta'_1,$$
$$\Delta\eta_1 = 0.9785 - 0.9748 = 0.37\%. \quad (21)$$

During buck mode,

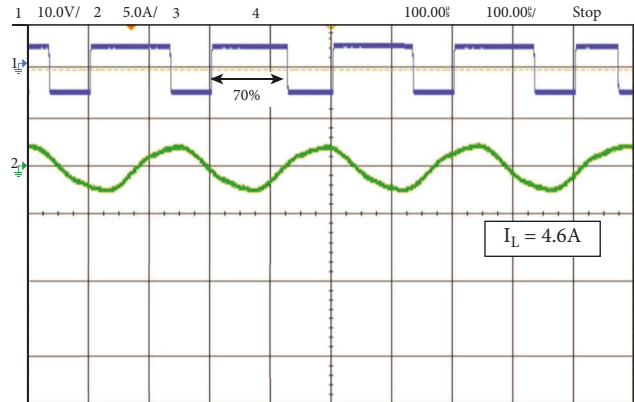$$\Delta\eta_2 = \eta_2 - \eta'_2 = \frac{7.1 \times 13.5}{21 \times 4.6}$$
$$- \frac{71 \times 13.35}{(21 \times 4.6) + [(1.7 \times 13.5) + (0.27 \times 4.6)]}, \quad (22)$$

$$\Delta\eta_2 = 0.992 - 0.793 = 19.87\%.$$

The proposed topology efficiency, passive elements, and switches are compared to other similar converter topologies in Table 3. The results show that the suggested converter's efficiency is comparable to that of other converters.
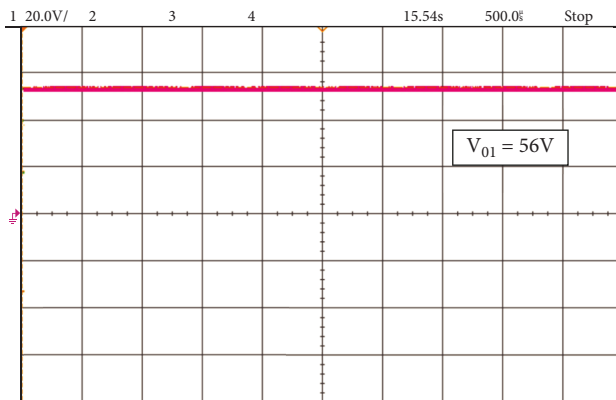
X-axis: Time (sec)
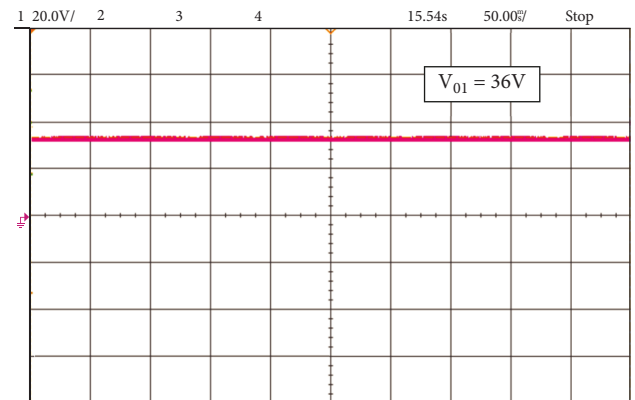Y-axis: Solar PV Voltage (V)

(a)

X-axis: Time (sec)
Y-axis: Inductor
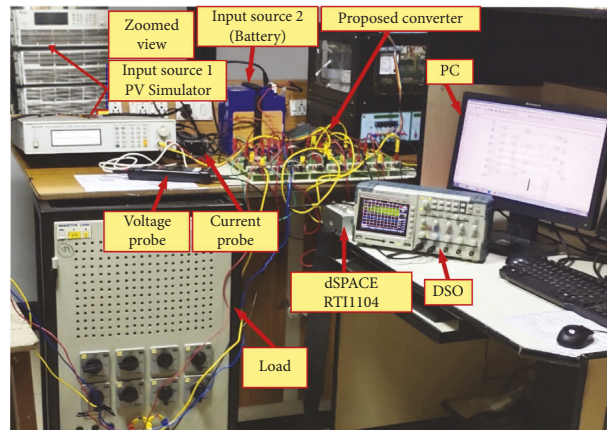current & Duty cycle

(b)

X-axis: Time (sec)
Y-axis: Output Voltage (V)

(c)

X-axis: Time (sec)
Y-axis: Output Voltage (V)

(d)

(e)

FIGURE 11: Experimental results of the proposed DIDO converter for state-3 and state-4 operation. (a) Solar PV and battery input voltage. (b) Duty cycle and inductor current. (c) Output voltage in state 3. (d) Output voltage in state 4. (e) Experimental setup.

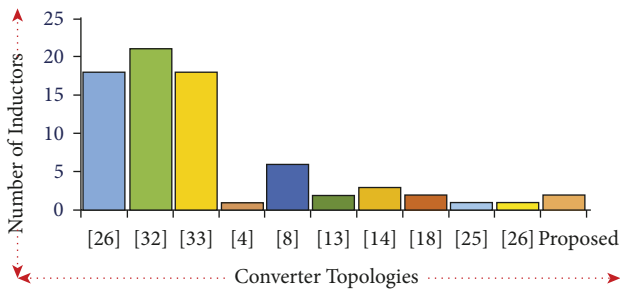TABLE 3: Component comparison with existing topologies.

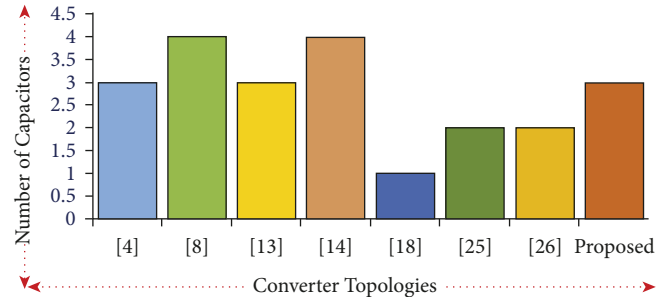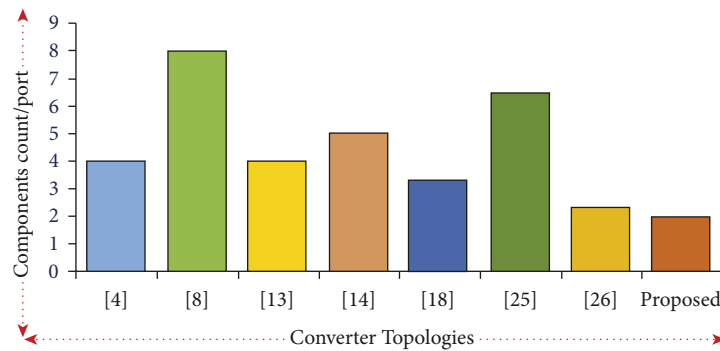| Topology	Inputs	Outputs	Inductors	Switches	Diodes	Capacitors	Components count per ports
[4]	1	1	1	4	—	3	4
[8]	1	1	6	6	—	4	8
[13]	1	1	2	1	2	3	4
[14]	1	1	3	1	2	4	5
[17]	2	1	2	5	2	1	3.33
[24]	1	1	1	5	5	2	6.5
[25]	1	2	1	4	—	2	2.33
Proposed	1 or 2	3 or 2	2	3	2	3	2
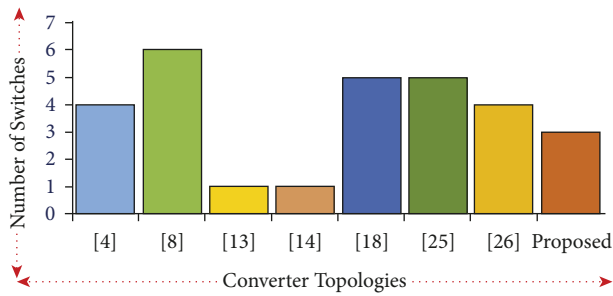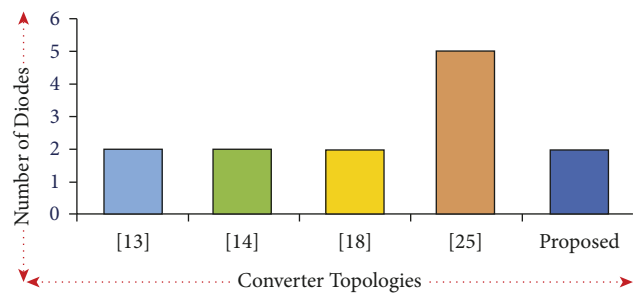
FIGURE 12: Comparison of various existing topologies with the proposed DIDO converter. (a) NS, (b) ND, (c) NL, (d) NC, and (e) CC/port.

Furthermore, the suggested converter provides advantages such as a modular structure with fewer components and the integration of a variety of input sources with varying voltage-current characteristics. This converter can be used in a high-voltage electric vehicle (HEV) power circuit. The proposed converter, in particular, can be used in a regenerative mode.

6. Conclusion

This study aims to create a DIDO (dual input, dual output) converter that can be used to integrate a variety of power sources into electric vehicles. This converter, in comparison to existing buck-boost converter topologies in the literature,

can produce buck, boost, and buck-boost output without the use of an additional transformer, and it can handle multiple resources of varying voltage and current capacity. To demonstrate the converter's functionality, a mathematical analysis was carried out. A simple control technique was used to control the power flow between the input sources. Finally, the converter's performance was evaluated using a low-voltage prototype model. The DIDO buck-boost topology that has been proposed has been successfully tested experimentally with a hardware setup.

Data Availability

No data were used to support the findings of the study.

Conflicts of Interest

The authors declare that there are no conflicts of interest on behalf of all authors.

References

[1] L. Wang, E. G. Collins, and H. Li, "Optimal design and real-time control for energy management in electric vehicles," *IEEE Transactions on Vehicular Technology*, vol. 60, no. 4, pp. 1419–1429, 2011.

[2] K. I. Hwu, K. W. Huang, and W. C. Tu, "Step-up converter combining KY and buck-boost converters," *Electronics Letters*, vol. 47, no. 12, pp. 722–724, 2011.

[3] S. Reddi Khasim and C. Dhanamjayulu, "Selection parameters and synthesis of multi-input converters for electric vehicles: an overview," *Renewable and Sustainable Energy Reviews*, vol. 141, Article ID 110804, 2021.

[4] N. Eskandarian, A. T. Harchegani, and S. S. Kazemi, "A novel structure for high step-up DC-DC converter with flexibility under the variable loads for EV solar charging system," *International Transactions on Electrical Energy Systems*, vol. 30, no. 6, Article ID e12375, 2020.

[5] M. Zandi, A. Payman, J.-P. Martin, S. Pierfederici, B. Davat, and F. Meibody-Tabar, "Energy management of a fuel cell/supercapacitor/battery power source for electric vehicular applications," *IEEE Transactions on Vehicular Technology*, vol. 60, no. 2, pp. 433–443, 2011.

[6] C.-C. Lin, L.-S. Yang, and G. W. Wu, "Study of a non-isolated bidirectional DC-DC converter," *IET Power Electronics*, vol. 6, no. 1, pp. 30–37, 2013.

[7] K. Kamalapathi, P. Srinivasa Rao Nayak, and V. K. Tyagi, "Design and implementation of dual-source (WPT+ PV) charger for EV battery charging," *International Transactions on Electrical Energy Systems*, vol. 31, no. 11, Article ID e13084, 2021.

[8] S. R. Khasim and C. Dhanamjayulu, *Design and Implementation of Asymmetrical Multilevel Inverter with Reduced Components and Low Voltage Stress*, IEEE Access, 3495–3511, 2022.

[9] A. Berigai Ramaiaha, R. Maurya, and S. R. Arya, "Bidirectional converter for electric vehicle battery charging with power quality features," *International Transactions on Electrical Energy Systems*, vol. 28, no. 9, Article ID e2589, 2018.

[10] P. Prabhakaran and V. Agarwal, "Novel four-port DC–DC converter for interfacing solar PV–fuel cell hybrid sources with low-voltage bipolar DC microgrids," *IEEE Journal of Emerging and Selected Topics in Power Electronics*, vol. 8, no. 2, pp. 1330–1340, 2020.

[11] C.-T. Tsai, T.-C. Liang, Y.-C. Kuo, and Y.-C. Luo, "An improved forward converter with PFC and ZVS features for split-phase charger applications," *Computers and Electrical Engineering*, vol. 51, pp. 291–303, 2016.

[12] S. R. Khasim, C. Dhanamjayulu, S. Padmanaban, J. B. Holm-Nielsen, and M. Mitolo, "A novel asymmetrical 21-level inverter for solar PV energy system with reduced switch count," *IEEE Access*, vol. 9, pp. 11761–11775, 2021.

[13] K. Suresh, N. Chellammal, C. Bharatiraja, P. Sanjeevikumar, F. Blaabjerg, and J. B. H. Nielsen, "Cost-efficient nonisolated three-port DC-DC converter for EV/HEV applications with energy storage," *International Transactions on Electrical Energy Systems*, vol. 29, no. 10, Article ID e12088, 2019.

[14] A. d. O. Ferreira, A. U. Brito, M. A. B. Galhardo, L. Ferreira, and W. N. Macêdo, "Modeling, control and simulation of a small photovoltaic-wind water pumping system without battery bank," *Computers and Electrical Engineering*, vol. 84, Article ID 106619, 2020.

[15] C. Dhanamjayulu, S. R. Khasim, S. Padmanaban, G. Arunkumar, J. B. Holm-Nielsen, and F. Blaabjerg, "Design and implementation of multilevel inverters for fuel cell energy conversion system," *IEEE Access*, vol. 8, pp. 183690–183707, 2020.

[16] S. R. Khasim and C. Dhanamjayulu, "Design of multiple input DC-DC converters for interfacing solar/fuel cell/battery electric vehicles," in *2021 Innovations in Power and Advanced Computing Technologies (I-PACT)*IEEE, 2021.

[17] H. Armghan, I. Ahmad, N. Ali, M. F. Munir, S. Khan, and A. Armghan, "Nonlinear controller analysis of fuel cell–battery–ultracapacitor-based hybrid energy storage systems in electric vehicles," *Arabian Journal for Science and Engineering*, vol. 43, no. 6, pp. 3123–3133, 2018.

[18] W. Rui, S. Qiuye, Z. Pinjia, G. Yonghao, Q. Dehao, and W. Peng, "Reduced-order transfer function model of the droop-controlled inverter via Jordan continued-fraction expansion," *IEEE Transactions on Energy Conversion*, vol. 35, no. 3, pp. 1585–1595, 2020.

[19] R. Wang, Q. Sun, P. Tu, J. Xiao, Y. Gui, and P. Wang, "Reduced-order aggregate model for large-scale converters with inhomogeneous initial conditions in DC microgrids," *IEEE Transactions on Energy Conversion*, vol. 36, no. 3, pp. 2473–2484, 2021.

[20] E. Babaei and H. M. Maheri, "Analytical solution for steady and transient states of buck dc–dc converter in CCM," *Arabian Journal for Science and Engineering*, vol. 38, no. 12, pp. 3383–3397, 2013.

[21] X. Hu, H. Zhang, D. Ma, R. Wang, and P. Tu, "Small leak location for intelligent pipeline system via action-dependent heuristic dynamic programming," *IEEE Transactions on Industrial Electronics*, vol. 69, no. 11, pp. 11723–11732, 2022.

[22] R. Wang, D. Ma, M.-J. Li, Q. Sun, H. Zhang, and P. Wang, "Accurate current sharing and voltage regulation in hybrid wind/solar systems: an adaptive dynamic programming approach," *IEEE Transactions on Consumer Electronics*, vol. 68, no. 3, pp. 261–272, 2022.

[23] Z. Zhao and A. Prodic, "Continuous-time digital controller for high-frequency DC-DC converters," *IEEE Transactions on Power Electronics*, vol. 23, no. 2, pp. 564–573, 2008.

[24] B. S. Naik, Y. Suresh, K. Aditya, and B. N. Rao, "A novel nine-level boost inverter with a low component count for electric vehicle applications," *International Transactions on Electrical Energy Systems*, vol. 31, no. 12, Article ID e13172, 2021.

[25] M. Rekik and L. Krichen, "Photovoltaic and plug-in electric vehicle for smart grid power quality enhancement," *Arabian Journal for Science and Engineering*, vol. 46, no. 2, pp. 1481–1497, 2021.

[26] A. K. Podder, N. K. Roy, H. R. Pota, and H. Roy Pota, "MPPT methods for solar PV systems: a critical review based on tracking nature," *IET Renewable Power Generation*, vol. 13, no. 10, pp. 1615–1632, 2019.

[27] E. Babaei, S. R. Nesaz, and K. J. Khasraghi, "Assessment of step-up dc–dc converter with high voltage ratio in different operational modes," *Arabian Journal for Science and Engineering*, vol. 39, no. 3, pp. 2033–2043, 2014.

[28] D. Chittathuru, S. Padmanaban, and R. Prasad, "Design and implementation of asymmetric cascaded multilevel inverter with optimal components," *Electric Power Components and Systems*, vol. 49, no. 4-5, pp. 361–374, 2021.